Supplementary Information

Y-substituted, nanocrystalline lanthanum tantalum oxide (n-LTO)

After synthesis and calcination at 923 K the oxide precursors (10 mol% Y, 25 mol% Y, 30 mol% Y) were nanocrystalline (Fig. S1 a)) and white as reported for n-LTO[1]. The synthesized Y-substituted n-LTO powders had specific surface areas between 9 m²/g and 14 m²/g which were slightly larger than that of n-LTO[1]. The morphologies of Y-substituted n-LTO (10 mol% Y, 25 mol% Y, 30 mol% Y) were similar to each other and had very small primary particles in the nm-range (Fig. S2 a)-c)). In contrast to m-$LaTaO_4$[1] and heavily Y-substituted m-$LaTaO_4$ (25 mol% Y and 30 mol% Y), 10 mol% Y-substituted m-$LaTaO_4$ ($La_{0.9}Y_{0.1}TaO_4$, Fig. S1 b)) was reproducibly single-phase after crystallization and could be refined in the monoclinic space group $P2_1/c$ (Fig. S1 b)). Synthesis of the two other Y-substituted m-$LaTaO_4$ (25 mol% Y, 30 mol% Y) samples resulted in two polymorphs which could be refined in the space groups $Cmc2_1$ and $P2_1/c$. The refinements of the HR-PXRD patterns revealed even a third phase (Fig. S3 a) and b)) which, however, was not observed by the XPS spectra of the Ta 4*f* region (Fig. S1 d)-f)). The fact that the third phase was only detected by HR-PXRD in the bulk sample can be explained by the surface-sensitivity of the XPS method resulting from the small mean-free path (normally between 1 and 10 nm[2]) of the photo-emitted electrons. The third phase was identified as $YTaO_4$ refined in the space group $P2/a$. The Vegard's plot shown in Figure S1 c) indicates a solubility limit of Y^{3+} in $LaTaO_4$ of approximately 10 mol% since the unit cell volumes of the samples with a nominal Y content of 25 mol% and 30 mol% did not differ much from that of the sample with 10 mol% Y. A similar solubility of Y has been previously observed in $Ca_{1-x}Y_xZrO_{3+0.5x}$.[3] Chemical analysis showed that the Y solubility of the oxynitrides $La_{1-x}Y_xTaO_2N$ (Fig. 2 a) exceeds ~10 mol% Y which was achieved for the 25 mol% and 30 mol% Y-substituted m-$La_{1-x}Y_xTaO_4$ (Tab. S2 a), b) and S3 a), b)). XPS measurements of the Ta 4*f* region of Y-substituted m-$LaTaO_4$ (10 mol% Y, 25 mol% Y, 30 mol% Y) were performed after treatment at 1673 K in order to have a Ta^{5+} reference. The XPS Ta 4*f* spectra of 25 mol% Y and 30 mol% Y were fitted with two binding states, while only one binding state was sufficient for $La_{0.9}Y_{0.1}TaO_4$ (Fig. S1 d)-f)). Hence, the presence of the two phases with space groups $Cmc2_1$ and $P2_1/c$ mentioned above was confirmed *via* the Ta 4*f* XPS data. The determined binding energies of the Ta $4f_{7/2}$ orbitals of all samples were in good agreement with already reported data of Ta(V)–O binding characters.[1,4,5] Since two binding states were sufficient to fit the data of the samples with Y contents of 25 mol% and 30 mol% despite the evidence of a third phase in the HR-PXRD patterns, the binding energy assignment was not entirely possible. The binding energies of the Ta $4f_{5/2}$ and the Ta $4f_{7/2}$ orbitals are listed in Table S4. Application of the Kubelka-Munk[6] function on the DRS measurement data revealed optical band gaps of $E_G = 4.5 \pm 0.1$ eV for Y-substituted n-LTO (10 mol% Y, 25 mol% Y, 30 mol% Y) (Fig. S4). These were good in agreement with the optical band gap of n-LTO[1] and m-$LaTaO_4$[1].

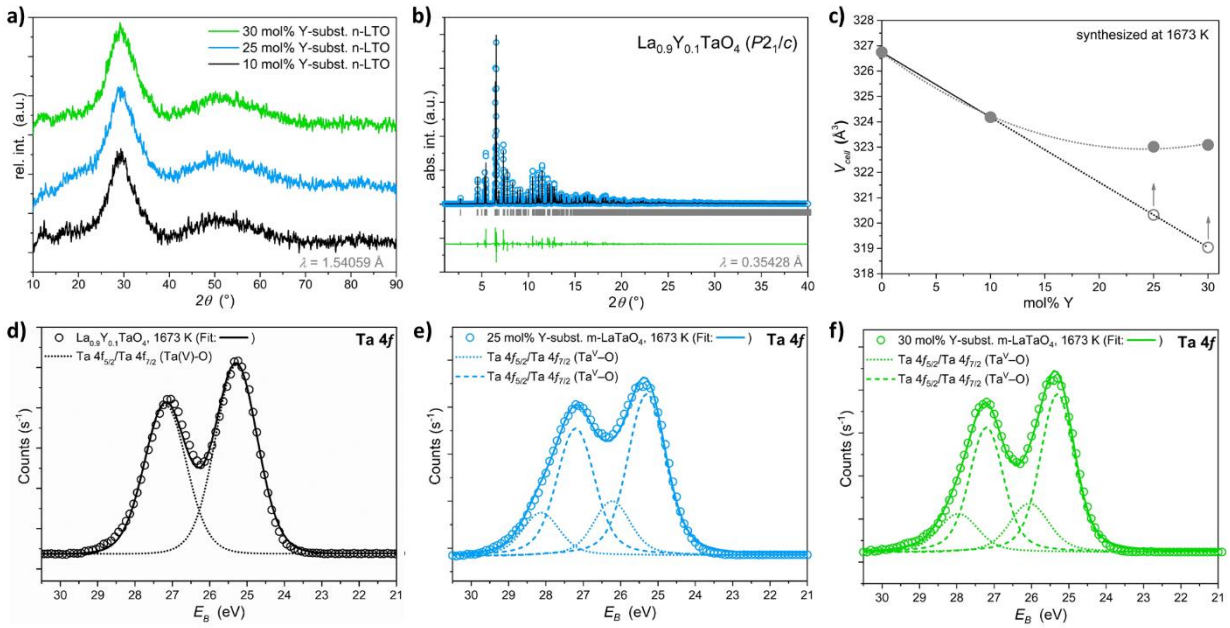

Fig. S1. a) PXRD patterns of Y-substituted nanocrystalline lanthanum tantalum oxide (n-LTO) (10 mol% Y, 25 mol% Y, 30 mol% Y) precursors. b) Rietveld refinements of the crystal structure of microcrystalline $La_{0.9}Y_{0.1}TaO_4$ in space group $P2_1/c$ from HR-PXRD data. c) Vegard's plot of the unit cell volumes of microcrystalline oxide precursors (10 mol% Y, 25 mol% Y, 30 mol% Y). The open circles represent the expected unit cell volume and the closed circles the determined unit cell volume. d)-f) XPS spectra of the Ta 4*f* region of Y-substituted microcrystalline $LaTaO_4$ (m-$LaTaO_4$) (10 mol% Y, 25 mol% Y, 30 mol% Y) samples treated at 1673 K. The solid line stands for the overall fit, the open circles represent the measurement data and the scattered lines are the fitting results of the Ta 4*f* orbitals.

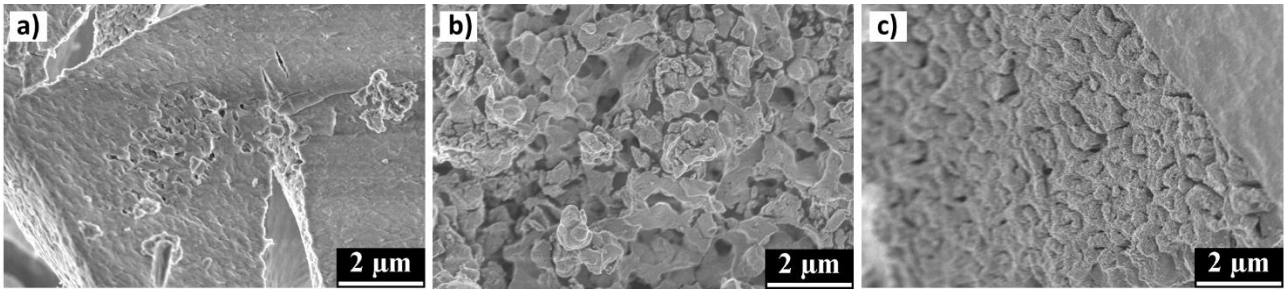

Fig. S2. SEM images of the white nanocrystalline Y-substituted n-LTO oxide precursors. a) 10 mol% Y. b) 25 mol% Y and c) 30 mol% Y.

Tab. S1. a) Unit cell parameters of m-$La_{0.9}Y_{0.1}TaO_4$.

Unit Cell Parameter	$La_{0.9}Y_{0.1}TaO_4$
***a* (Å)**	7.63033(8)
***b* (Å)**	5.55665(6)
***c* (Å)**	7.79671(8)
***β* (°)**	101.2852(6)
V_{cell} **(Å³)**	324.181(6)
Space group	$P2_1/c$
Phase fraction (wt.-%)	100
R_p **(%)**	11.2
R_{wp} **(%)**	14.9
χ^2	10.6
R_{Bragg} **(%)**	8.81

Tab. S1. b) Refined atom positions of m-$La_{0.9}Y_{0.1}TaO_4$ in space group $P2_1/c$ synthesized at 1673 K.

Atom	Wyck. Symb.	*x*	*y*	*z*	B_{iso} (Å²)	sof.[a]
La	4*e*	0.34351(2)	0.7724(5)	0.09718(2)	1.013(4)	0.9[b]
Y	4*e*	0.34351(2)	0.7724(5)	0.09718(2)	1.013(4)	0.1[b]
Ta	4*e*	0.16824(1)	0.2652(3)	0.30151(2)	0.820(2)	1[b]
O(1)	4*e*	0.161(2)	0.153(2)	0.043(2)	1[b]	1[b]
O(2)	4*e*	0.062(2)	0.584(3)	0.216(2)	1[b]	1[b]
O(3)	4*e*	0.377(2)	0.468(3)	0.333(2)	1[b]	1[b]
O(4)	4*e*	0.343(2)	0.009(3)	0.359(2)	1[b]	1[b]

[a]site occupation factor, [b]fixed

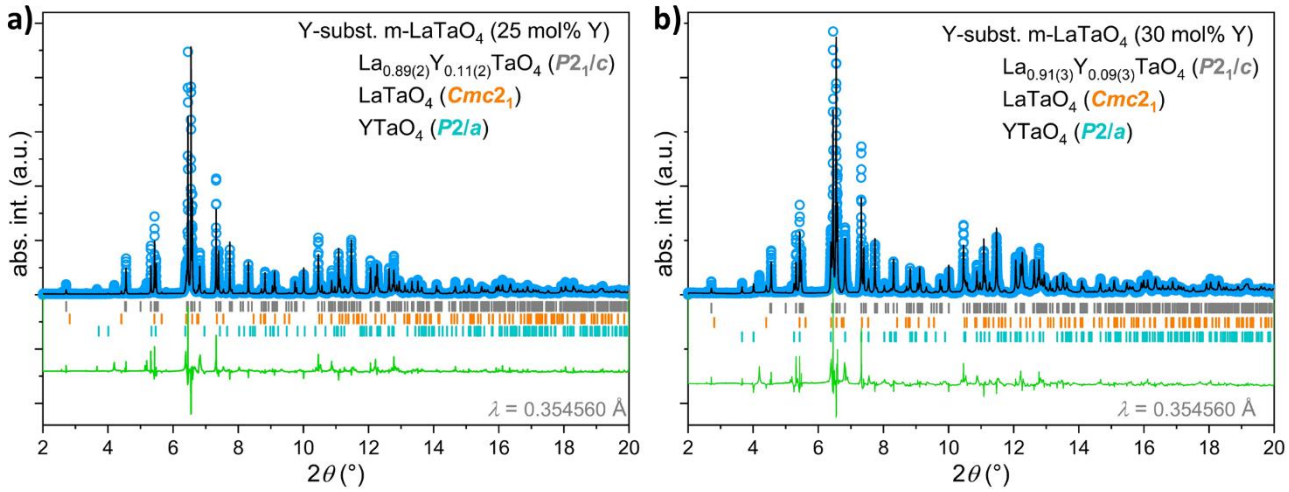

Fig. S3. Rietveld refinements of the HR-PXRD data of a) Y-substituted m-$LaTaO_4$ (25 mol% Y) and b) Y-substituted m-$LaTaO_4$ (30 mol% Y). The reflection positions of $LaTaO_4$ in the space group $Cmc2_1$ are marked in violet and those of $La_{1-x}Y_xTaO_4$ in the space group $P2_1/c$ in gray. The reflections of the third phase $YTaO_4$ in space group *P2/a* are marked in blue.

Tab. S2. a) Unit cell parameters of both polymorphs of Y-substituted m-$LaTaO_4$ (25 mol% Y) and $YTaO_4$ synthesized at 1673 K (HR-PXRD data).

Unit Cell Parameter	$La_{0.89(2)}Y_{0.11(2)}TaO_4$	$LaTaO_4$	$YTaO_4$
a **(Å)**	7.63354(2)	3.8792(5)	5.3534(2)
b **(Å)**	5.55541(2)	14.3987(2)	5.4682(2)
c **(Å)**	7.79508(2)	5.9953(7)	5.1089(2)
β **(°)**	101.2300(2)	90	97.318(2)
V_{cell} **(Å³)**	324.240(2)	334.87(7)	148.34(8)
Space group	$P2_1/c$	$Cmc2_1$	$P2/a$
Phase fraction (wt.-%)	90.12(1)	7.54(3)	2.34(2)
R_p **(%)**		19.5	
R_{wp} **(%)**		25.3	
χ^2		27.9	
R_{Bragg} **(%)**	16.6	42.5	66.0

Tab. S2. b) Refined atom positions of $La_{0.89(2)}Y_{0.11(2)}TaO_4$ in space group $P2_1/c$ in Y-substituted m-$LaTaO_4$ (25 mol% Y).

Atom	Wyck. Symb.	*x*	*y*	*z*	B_{iso} (Å²)	sof.[a]
La	4*e*	0.3430(4)	0.7729(1)	0.0966(4)	1.030(1)	0.89(2)
Y	4*e*	0.3430(4)	0.7729(1)	0.0966(4)	1.030(1)	0.11(2)
Ta	4*e*	0.1652(3)	0.2635(1)	0.3042(3)	1.054(8)	1[c]
O(1)	4*e*	0.175[b]	0.157[b]	0.052[b]	2[c]	1[c]
O(2)	4*e*	0.052[b]	0.589[b]	0.207[b]	2[c]	1[c]
O(3)	4*e*	0.381[b]	0.485[b]	0.335[b]	2[c]	1[c]
O(4)	4*e*	0.334[b]	0.009[b]	0.381[b]	2[c]	1[c]

[a]site occupation factor, [b]adopted from Kurova *et al.*[7], [c]fixed

Tab. S2. c) Refined atom positions of $LaTaO_4$ in space group $Cmc2_1$ in Y-substituted m-$LaTaO_4$ (25 mol% Y).

Atom	Wyck. Symb.	*x*	*y*	*Z*	B_{iso} (Å²)	sof.[a]
La	4*a*	0	0.1755(2)	0.3971(2)	1[c]	1[c]
Ta	4*a*	0	0.4129(1)	0.3266(2)	1[c]	1[c]
O(1)	4*a*	0	0.304[b]	0.408[b]	2[c]	1[c]
O(2)	4*a*	0	0.331[b]	0.871[b]	2[c]	1[c]
O(3	4*a*	0	0.470[b]	0.532[b]	2[c]	1[c]
O(4)	4*a*	0	0.915[b]	0.250[b]	2[c]	1[c]

[a]site occupation factor, [b]adopted from Titov *et al.*[8], [c]fixed

Tab. S2. d) Refined atom positions of $YTaO_4$ in space group *P2/a* in Y-substituted m-$LaTaO_4$ (25 mol% Y).

Atom	Wyck. Symb.	*x*	*y*	*z*	B_{iso} (Å²)	sof.[a]
Y	2*f*	¼	0.739(2)	0	1[c]	1[c]
Ta	2*e*	¼	0.207(9)	½	1[c]	1[c]
O(1)	4*g*	0.489[b]	0.434[b]	0.268[b]	2[c]	1[c]
O(2)	4*g*	0.102[b]	0.084[b]	0.252[b]	2[c]	1[c]

[a]site occupation factor, [b]adopted from Brixner *et al.*[9], [c]fixed

Tab. S3. a) Unit cell parameters of both polymorphs of Y-substituted m-$LaTaO_4$ (30 mol%) and $YTaO_4$ synthesized at 1673 K (HR-PXRD data).

Unit Cell Parameter	$La_{0.91(3)}Y_{0.09(3)}TaO_4$	$LaTaO_4$	$YTaO_4$
***a* (Å)**	7.6326(2)	3.8454(2)	5.4159(6)
***b* (Å)**	5.5559(2)	14.540(6)	5.5545(7)
***c* (Å)**	7.7950(3)	6.008(2)	5.0900(5)
***β* (°)**	101.245(2)	90	95.473(9)
V_{cell} **(Å³)**	324.209(2)	335.9(3)	152.42(3)
Space group	$P2_1/c$	$Cmc2_1$	*P2/a*
Phase fraction (wt.-%)	79.29(8)	3.03(2)	17.68(4)
R_p **(%)**		17.6	
R_{wp} **(%)**		23.6	
χ^2		20.2	
R_{Bragg} **(%)**	13.4	38.2	33.1

Tab. S3. b) Refined atom positions of $La_{0.913(3)}Y_{0.09(3)}TaO_4$ in space group $P2_1/c$ in Y-substituted m-$LaTaO_4$ (30 mol% Y).

Atom	Wyck. Symb.	*x*	*y*	*z*	B_{iso} (Å²)	sof.[a]
La	4*e*	0.3436(5)	0.7717(1)	0.0973(5)	1.651(2)	0.91(3)
Y	4*e*	0.3436(5)	0.7717(1)	0.0973(5)	1.651(2)	0.09(3)
Ta	4*e*	0.1663(4)	0.2621(1)	0.3038(4)	1.805(9)	1[c]
O(1)	4*e*	0.175[b]	0.157[b]	0.052[b]	2[c]	1[c]
O(2)	4*e*	0.052[b]	0.589[b]	0.207[b]	2[c]	1[c]
O(3)	4*e*	0.381[b]	0.485[b]	0.335[b]	2[c]	1[c]
O(4)	4*e*	0.334[b]	0.009[b]	0.381[b]	2[c]	1[c]

[a]site occupation factor, [b]adopted from Kurova *et al.*[7], [c]fixed

Tab. S3. c) Refined atom positions of $LaTaO_4$ in space group $Cmc2_1$ in Y-substituted m-$LaTaO_4$ (30 mol% Y).

Atom	Wyck. Symb.	*x*	*y*	*z*	B_{iso} (Å²)	sof.[a]
La	4*a*	0	0.253(5)	0.170(6)	1[c]	1[c]
Ta	4*a*	0	0.447(3)	0.532(5)	1[c]	1[c]
O(1)	4*a*	0	0.304[b]	0.408[b]	2[c]	1[c]
O(2)	4*a*	0	0.331[b]	0.871[b]	2[c]	1[c]
O(3)	4*a*	0	0.470[b]	0.532[b]	2[c]	1[c]
O(4)	4*a*	0	0.915[b]	0.250[b]	2[c]	1[c]

[a]site occupation factor, [b]adopted from Titov *et al.*[8], [c]fixed

Tab. S3. d) Refined atom positions of $YTaO_4$ in space group *P2/a* in Y-substituted m-$LaTaO_4$ (30 mol% Y).

Atom	Wyck. Symb.	*x*	*y*	*z*	B_{iso} (Å²)	sof.[a]
Y	2*f*	¼	0.734(4)	0	1[c]	1[c]
Ta	2*e*	¼	0.286(2)	½	1[c]	1[c]
O(1)	4*g*	0.489[b]	0.434[b]	0.268[b]	2[c]	1[c]
O(2)	4*g*	0.102[b]	0.084[b]	0.252[b]	2[c]	1[c]

[a]site occupation factor, [b]adopted from Brixner *et al.*[9], [c]fixed

Tab. S4. Binding energies of the Ta $4f_{5/2}$ and the respective Ta $4f_{7/2}$ orbitals of Y-substituted m-$LaTaO_4$ (10 mol% Y, 25 mol% Y, 30 mol% Y).

Compound	$E_{B.Ta\ 4f5/2}$ (eV)	$E_{B.Ta\ 4f7/2}$ (eV)
$La_{0.9}Y_{0.1}TaO_4$	27.2	25.3
Y-substituted m-$LaTaO_4$ (x_Y = 25 mol%)	28.0	26.1
	27.2	25.3
Y-substituted m-$LaTaO_4$ (x_Y = 30 mol%)	27.1	25.2
	28.1	26.2

DRS spectra of the oxide precursors Y-subst. n-LTO and nanocrystalline yttrium tantalum oxide (n-YTO)

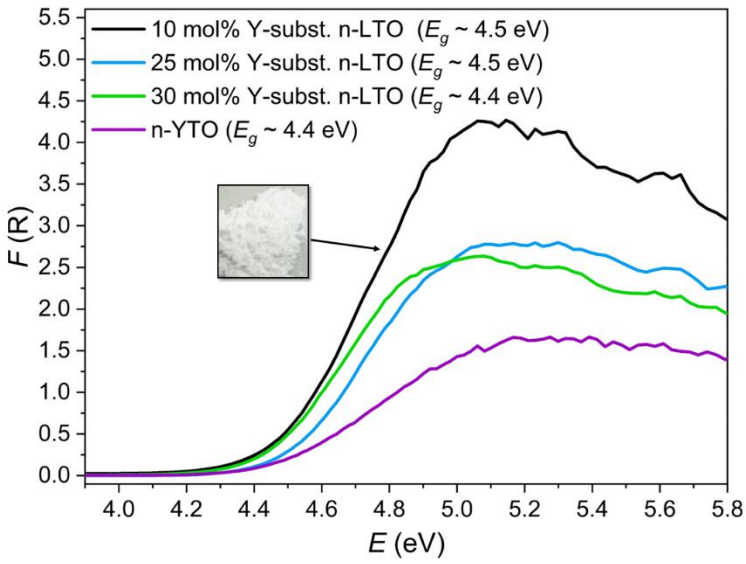

Fig. S4. Diffuse reflectance spectra - converted to a Kubelka-Munk[6] plot - of Y-substituted n-LTO (10 mol% Y, 25 mol% Y, 30 mol% Y) and n-YTO.

Oxynitrides $La_{1-x}Y_xTaO_2N$

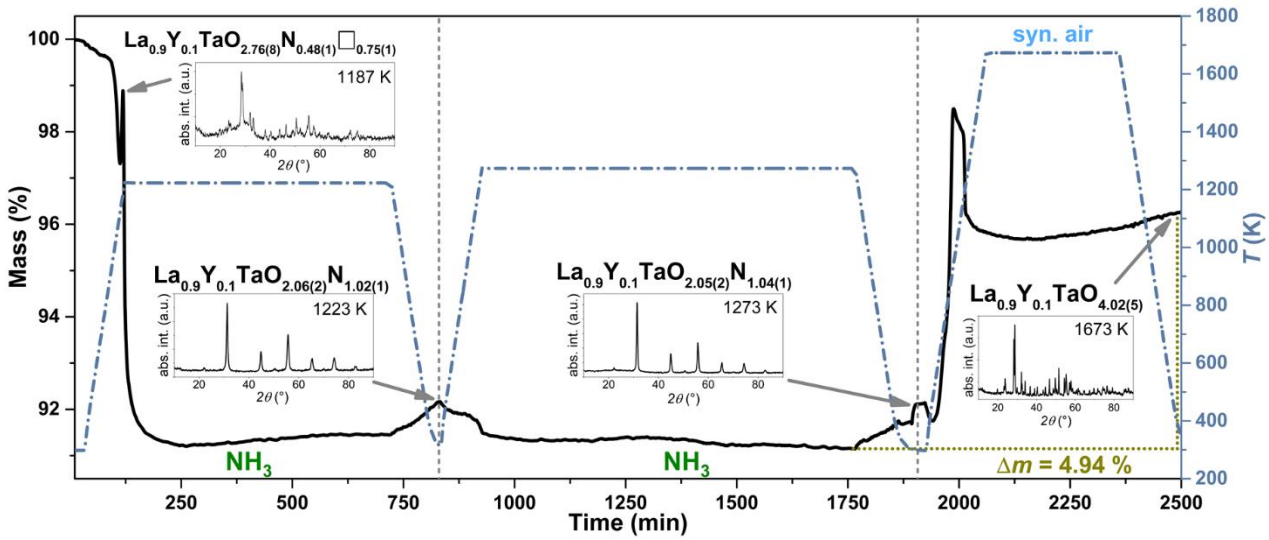

Fig. S5. TGA of *in situ* experiments of the ammonolysis of 10 mol% Y-substituted n-LTO (10 vol.% Ar in NH_3) and the subsequent reoxidation of $La_{0.9}Y_{0.1}TaO_2N$ with heating and cooling rates of 10 K/min. The displayed PXRD patterns and the anionic compositions were measured *ex situ* after specific termination experiments. The formation of the oxynitride is effected by means of the intermediate $La_{0.9}Y_{0.1}Ta^{IV}O_{2.76(8)}N_{0.48(1)}\square_{0.75(9)}$ (1187 K) suggesting a soft topotactic reaction[1] to $La_{0.9}Y_{0.1}Ta^{IV}O_2N$.

Crystal structure analysis of the intermediate $La_{0.9}Y_{0.1}TaO_{2.76(8)}N_{0.48(1)}\square_{0.75(9)}$

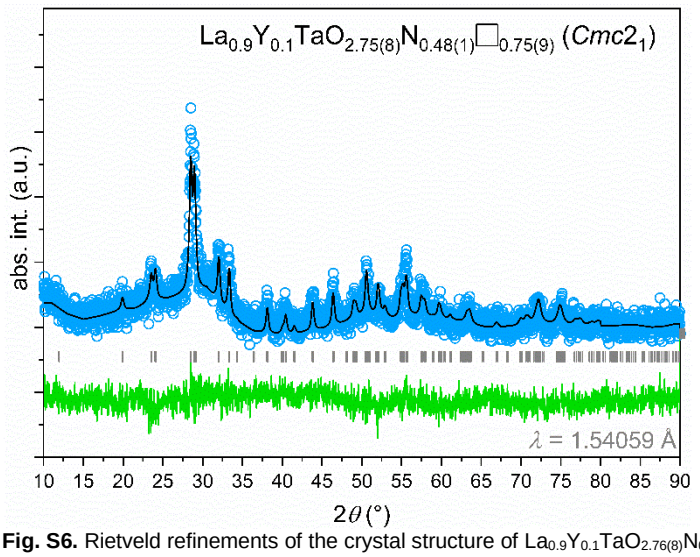

Fig. S6. Rietveld refinements of the crystal structure of $La_{0.9}Y_{0.1}TaO_{2.76(8)}N_{0.48(1)}\square_{0.75(9)}$ in space group type $Cmc2_1$.

Tab. S5. a) Unit cell parameters of $La_{0.9}Y_{0.1}TaO_{2.76(8)}N_{0.48(1)}\square_{0.75(9)}$ in space group type $Cmc2_1$.

Unit Cell Parameter	$La_{0.9}Y_{0.1}TaO_{2.76(8)}N_{0.48(1)}\square_{0.75(9)}$
a **(Å)**	3.9140(8)
b **(Å)**	14.806(4)
c **(Å)**	5.5897(2)
V_{cell} **(Å³)**	323.94(2)
Space group	$Cmc2_1$
R_p **(%)**	7.29
R_{wp} **(%)**	9.16
χ^2	1.09
R_{Bragg} **(%)**	9.12

Tab. S5. b) Atom positions of $La_{0.9}Y_{0.1}TaO_{2.76(8)}N_{0.48(1)}\square_{0.75(9)}$ in space group type *Cmc*2_1.

Atom	Wyck. Symb.	*x*	*y*	*z*	B_{iso} (Å²)	sof.[a]
La	4*a*	0	0.1713(1)	0.26(4)	2[b]	0.9[b]
Y	4*a*	0	0.1713(1)	0.26(4)	2[b]	0.1[b]
Ta	4*a*	0	0.4152(2)	0.29(4)	2[b]	1[b]
O(1)	4*a*	0	0.353(2)	0.36(5)	1[b]	1[b]
O(2)	4*a*	0	0.296(2)	1.00(6)	1[b]	1[b]
O(3)	4*a*	0	0.485(1)	0.66(5)	1[b]	1[b]
O(4)	4*a*	0	0.914(1)	0.250[b]	1[b]	1[b]

[a]site occupancy factor, [b]fixed

Crystal structure analysis of $La_{1-x}Y_xTaO_2N$

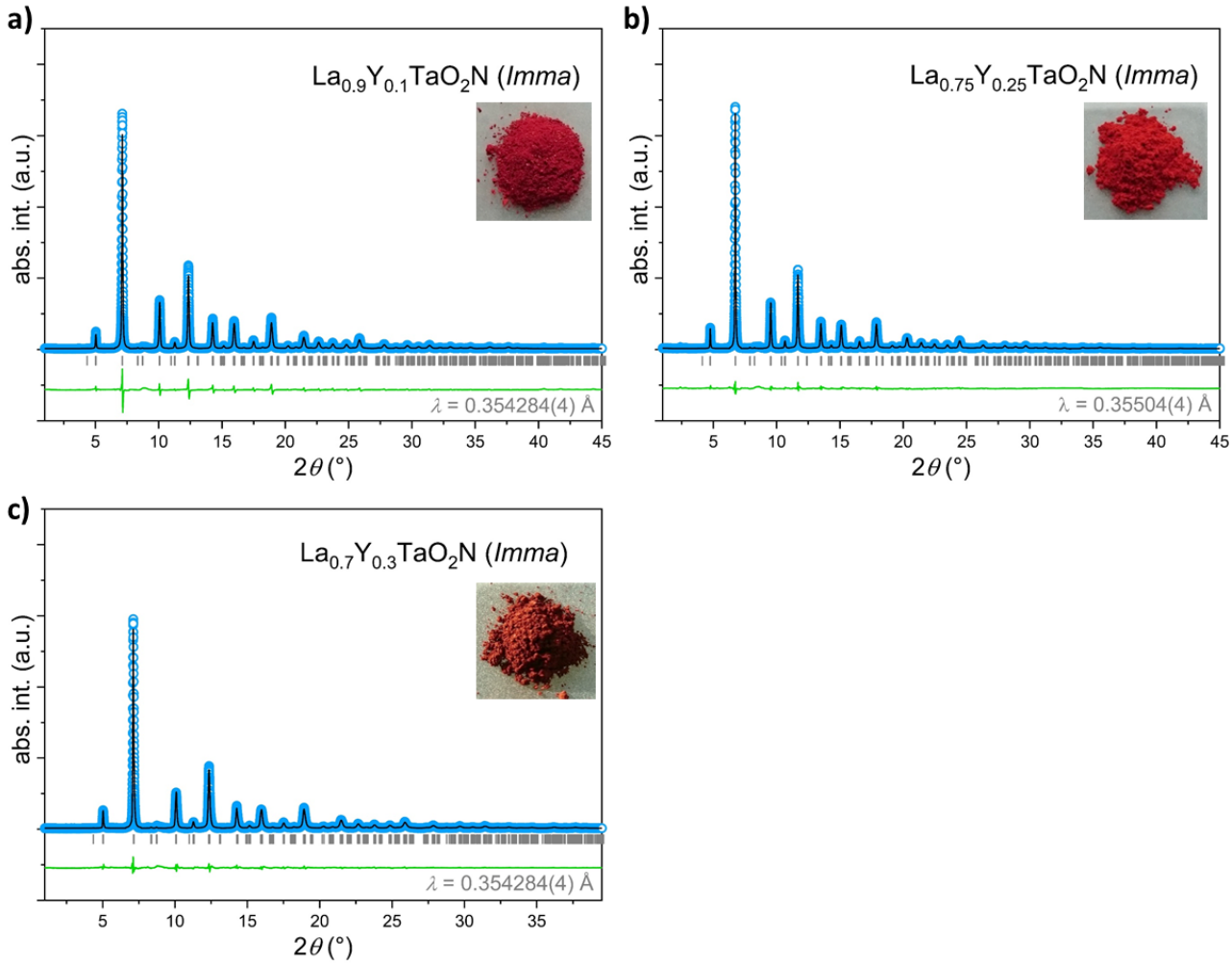

Fig. S7. a)-c) Rietveld refinements of the crystal structure of $La_{1-x}Y_xTaO_2N$ (x = 0.1, 0.25, 0.3) with the respective powder images.

Tab. S6. a) Unit cell parameters of $La_{1-x}Y_xTaO_2N$ (x = 0.1, 0.25, 0.3) from HR-PXRD data.

Unit Cell Parameter	$La_{0.9}Y_{0.1}TaO_2N$	$La_{0.75}Y_{0.25}TaO_2N$	$La_{0.7}Y_{0.3}TaO_2N$
***a* (Å)**	5.7093(2)	5.6993(5)	5.7044(2)
***b* (Å)**	8.0563(2)	8.0845(3)	8.0908(2)
***c* (Å)**	5.7322(2)	5.6901(6)	5.6709(2)
V_{cell} **(Å³)**	263.66(1)	262.18(4)	261.73(2)
Space group	*Imma*	*Imma*	*Imma*
Phase fraction (wt.-%)	100	100	100
R_p **(%)**	5.56	6.17	7.71
R_{wp} **(%)**	9.47	9.60	11.4
χ^2	4.72	4.65	5.76
R_{Bragg} **(%)**	3.94	4.14	19.5

Tab. S6. b) Refined atom positions of $La_{0.9}Y_{0.1}TaO_2N$ from HR-PXRD data (space group: *Imma*).

Atom	Wyck. Symb.	*x*	*y*	*z*	B_{iso} (Å²)	sof.[a]
La	4*e*	0	¼	0.5[c]	0.735(1)	0.9[d]
Y	4*e*	0	¼	0.5[c]	0.735(1)	0.1[d]
Ta	4*a*	0	0	0	0.332(1)	1[d]
O(1)	4*e*	0	¼	0.090(5)	2.645(2)[b]	⅔[d]
N(1)	4*e*	0	¼	0.090(5)	2.645(2)[b]	⅓[d]
O(2)	8*g*	¼	0.978(2)	¼	2.645(2)[b]	⅔[d]
N(2)	8*g*	¼	0.978(2)	¼	2.645(2)[b]	⅓[d]

[a]site occupancy factor, [b]constrained, [c]fixed according to Porter *et al.*[10], [d]fixed

Tab. S6. c) Refined atom positions of $La_{0.75}Y_{0.25}TaO_2N$ from HR-PXRD data (space group: *Imma*).

Atom	Wyck. Symb.	*x*	*y*	*z*	B_{iso} (Å²)	sof.[a]
La	4*e*	0	¼	0.5[c]	0.986(1)	0.75[d]
Y	4*e*	0	¼	0.5[c]	0.986(1)	0.25[d]
Ta	4*a*	0	0	0	0.405(1)	1[d]
O(1)	4*e*	0	¼	0.083(7)	3.345(3)[b]	⅔[d]
N(1)	4*e*	0	¼	0.083(7)	3.345(3)[b]	⅓[d]
O(2)	8*g*	¼	0.970(3)	¼	3.345(3)[b]	⅔[d]
N(2)	8*g*	¼	0.970(3)	¼	3.345(3)[b]	⅓[d]

[a]site occupancy factor, [b]constrained, [c]fixed according to Porter *et al.*[10], [d]fixed

Tab. S6. d) Refined atom positions of $La_{0.7}Y_{0.3}TaO_2N$ from HR-PXRD data (space group: *Imma*).

Atom	Wyck. Symb.	*x*	*y*	*z*	B_{iso} (Å²)	sof.[a]
La	4*e*	0	¼	0.5[c]	0.910(2)	0.7[d]
Y	4*e*	0	¼	0.5[c]	0.910(2)	0.3[d]
Ta	4*a*	0	0	0	0.364(1)	1[d]
O(1)	4*e*	0	¼	0.075(6)	3.473(4)[b]	⅔[d]
N(1)	4*e*	0	¼	0.075(6)	3.473(4)[b]	⅓[d]
O(2)	8*g*	¼	0.973(4)	¼	3.473(4)[b]	⅔[d]
N(2)	8*g*	¼	0.973(4)	¼	3.473(4)[b]	⅓[d]

[a]site occupancy factor, [b]constrained, [c]fixed according to Porter *et al.*[10], [d]fixed

Neutron diffraction

Since $LaTaON_2$[1,11,12] at room temperature was reported to be either orthorhombic (space group *Imma*) or monoclinic (*C*2/*m* or equivalent *I*2/*m*) and $LaTaO_2N$ only orthorhombic (*Imma*)[1], the ND data were refined by using both space group types. In accordance with the HR-PXRD results, refinements of the ND data (Fig. S8) were also most robust by using the *Imma* space group resulting in the lowest χ^2 value. Unfortunately, the limited ND data quality owing to the small sample size of only 200 mg (obtained after *ex situ* ammonolysis) and contributions from the sample container (vanadium can) did not allow precise determination of the anionic composition of $La_{0.9}Y_{0.1}TaO_2N$ by means of the occupancy factors combined with high B_{iso} values.

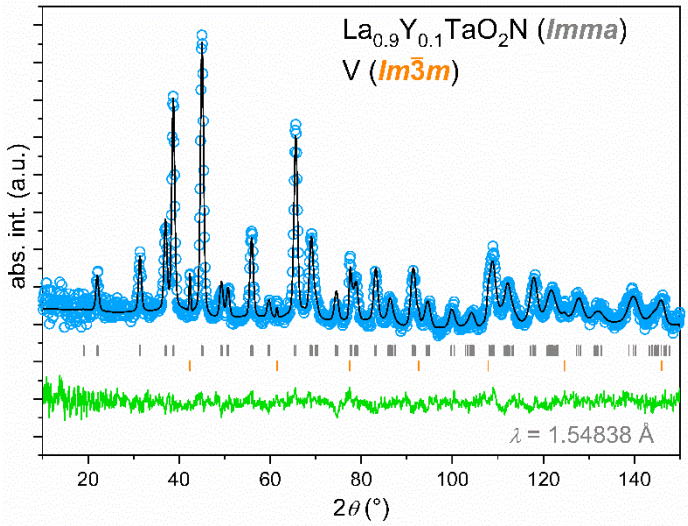

Fig. S8. Rietveld refinements of the ND data of $La_{0.9}Y_{0.1}TaO_2N$. The compound was synthesized under flowing ammonia at 1223 K for 10 h.

Tab. S7. a) Unit cell parameters of $La_{0.9}Y_{0.1}TaO_2N$ from ND data (space group: *Imma*).

Unit Cell Parameter	$La_{0.9}Y_{0.1}TaO_2N$	V
a **(Å)**	5.716(2)	3.0303(7)
b **(Å)**	8.059(3)	3.0303(7)
c **(Å)**	5.740(3)	3.0303(7)
V_{cell} **(Å³)**	264.41(2)	27.825(1)
Space group	*Imma*	$Im\bar{3}m$
Phase fraction (wt.-%)	45.92(2)	54.08(5)
R_p **(%)**	2.46	
R_{wp} **(%)**	3.21	
χ^2	4.94	
R_{Bragg} **(%)**	10.6	93.3

Tab. S7. b) Refined atom positions of $La_{0.9}Y_{0.1}TaO_2N$ from ND data (space group: *Imma*).

Atom	Wyck. Symb.	*x*	*y*	*z*	B_{iso} (Å²)	sof.[a]
La	4*e*	0	¼	0.495(5)	2.6(2)	0.9[b]
Y	4*e*	0	¼	0.495(5)	2.6(2)	0.1[b]
Ta	4*a*	0	0	0	2.0(2)	1[b]
O(1)	4*e*	0	¼	0.076(2)	1.9(1)	⅔[b]
N(1)	4*e*	0	¼	0.076(2)	1.9(1)	⅓[b]
O(2)	8*g*	¼	0.964(1)	¼	1.9(1)	⅔[b]
N(2)	8*g*	¼	0.964(1)	¼	1.9(1)	⅓[b]

[a]site occupancy factor, [b]fixed

Tab. S7. c) Unit cell parameters of $La_{0.9}Y_{0.1}TaON_2$ as alternative structure model (space group: *Imma*).

Unit Cell Parameter	$La_{0.9}Y_{0.1}TaON_2$	V
***a* (Å)**	5.712(2)	3.0283(5)
***b* (Å)**	8.061(3)	3.0283(5)
***c* (Å)**	5.732(2)	3.0283(5)
V_{cell} **(Å³)**	263.9(1)	27.771(8)
Space group	*Imma*	$Im\bar{3}m$
Phase fraction (wt.-%)	21(5)	79(27)
R_p **(%)**	2.30	
R_{wp} **(%)**	2.93	
χ^2	4.00	
R_{Bragg} **(%)**	10.7	44.0

Tab. S7. d) Refined atom positions from ND data using $La_{0.9}Y_{0.1}TaON_2$ as alternative structure model (space group: *Imma*).

Atom	Wyck. Symb.	*x*	*y*	*z*	B_{iso} (Å²)	sof.[a]
La(1)	4*e*	0	¼	0.5[c]	1[b]	0.9[b]
Y(1)	4*e*	0	¼	0.5[c]	1[b]	0.1[b]
Ta(1)	4*a*	0	0	0	1[b]	1[b]
O(1)	4*e*	0	¼	0.076(2)	0.6(2)	0.55(9)
N(1)	4*e*	0	¼	0.076(2)	0.6(2)	0.45(9)
O(2)	8*g*	¼	0.9636(9)	¼	3.4(2)	0.05(7)
N(2)	8*g*	¼	0.9636(9)	¼	3.4(2)	0.95(7)

[a]site occupancy factor, [b]fixed, [c]fixed according to Porter *et al.*[10]

Bond length and angle analysis by Rietveld refinements

Tab. S8. a) Ta–*X*–Ta angles and average Ta-*X*-Ta angle of $La_{1-x}Y_xTaO_2N$ (x = 0, 0.1, 0.25, 0.3) *via* Rietveld refinements of the respective HR-PXRD data.

Compound	$LaTaO_2N$[1]	$La_{0.9}Y_{0.1}TaO_2N$	$La_{0.75}Y_{0.25}TaO_2N$	$La_{0.7}Y_{0.3}TaO_2N$
$\measuredangle_{Ta-X1-Ta}$ (°)	153.7(2)	151.3(3)	153.7(4)	149.6(2)
$\measuredangle_{Ta-X2-Ta}$ (°)	169.99(6)	169.98(6)	166.26(1)	165.33(8)
$\measuredangle_{average}$ (°)	161.85(8)	160.65(8)	160.0(5)	157.47(9)

Tab. S8. b). Distances in the $Ta(O,N)_6$ octahedron of $La_{1-x}Y_xTaO_2N$ (x = 0[1], 0.1, 0.25, 0.3) *via* Rietveld refinements of the respective HR-PXRD data.

Compound	$LaTaO_2N$[1]	$La_{0.9}Y_{0.1}TaO_2N$	$La_{0.75}Y_{0.25}TaO_2N$	$La_{0.7}Y_{0.3}TaO_2N$
$d_{Ta-(O,N)1}$ (Å)	2.0428(2)[1]	2.0420(2)	2.0260(1)	2.0263(1)
$d_{Ta-(O,N)2}$ (Å)	2.0428(2)[1]	2.0420(2)	2.0260(1)	2.0263(1)
$d_{Ta-(O,N)3}$ (Å)	2.0428(2)[1]	2.0420(2)	2.0260(1)	2.0263(1)
$d_{Ta-(O,N)4}$ (Å)	2.0428(2)[1]	2.0420(2)	2.0260(1)	2.0263(1)
$d_{Ta-(O,N)5}$ (Å)	2.0799(7)[1]	2.1113(7)	2.1263(5)	2.1664(6)
$d_{Ta-(O,N)6}$ (Å)	2.0799(7)[1]	2.1113(7)	2.1263(5)	2.1664(6)
$d_{Ta-(O,N),average}$ (Å)	2.0551(7)	2.0651(4)	2.0594(6)	2.0730(2)

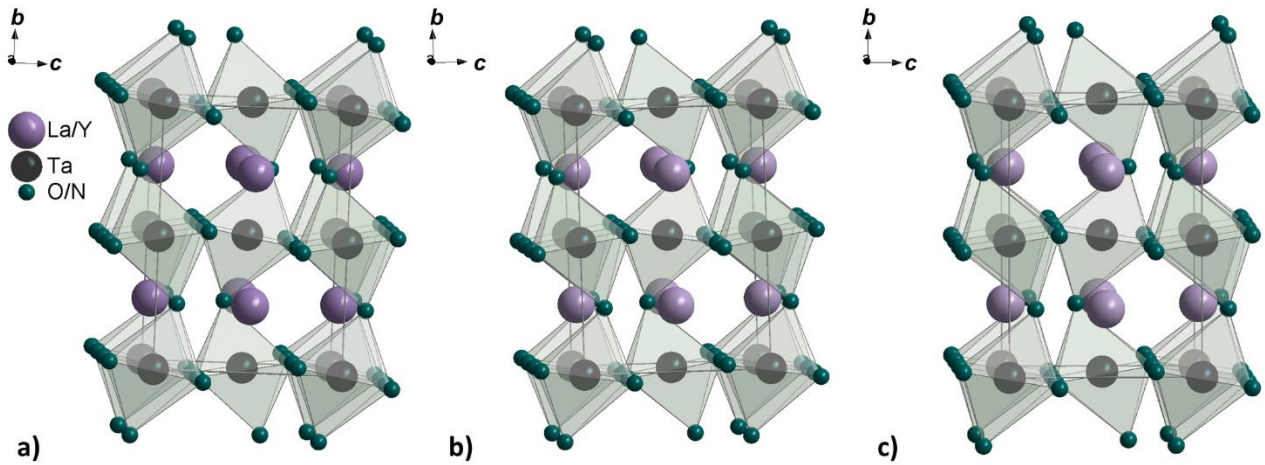

Fig. S9. Section of the crystal structure of a) $La_{0.9}Y_{0.1}TaO_2N$, b) $La_{0.75}Y_{0.25}TaO_2N$, and c) $La_{0.7}Y_{0.3}TaO_2N$ based on the results obtained *via* Rietveld refinements.

Determination of band edges

To determine the band edge positions of $La_{1-x}Y_xTa^{IV}O_2N$ Mott-Schottky-analyses were carried out. However, none of these experiments were successful, because either the particulate films were detached by the electrolyte from the substrate or the grain boundary resistance was exceeding the accessible range. Additionally, the experimental determination of the band edge positions is challenging due to the fact that the classical Mott-Schottky-analysis is often not straightforward for particle-based films of oxides or even oxynitrides.[13] Since experimental attempts to measure the band edge positions failed, an approach based on the absolute electronegativities of the constituent elements to calculate the band edge positions was used.[14] This was previously successfully applied to $CaTaO_2N$.[15] For $La_{1-x}Y_xTaO_2N$ ($x \leq 0.3$) and $LaTaON_2$ the calculated values for E_{CBM} and E_{VBM} are summarized in Table S9 together with those of $CaTaO_2N$ as calculated reference. In the latter case the calculated and the reported value agree very well. By comparing $LaTa^{V}ON_2$ and $LaTa^{IV}O_2N$ two things become obvious: i) interestingly the CBM position is nearly unaffected by the valence change from Ta^{5+} to Ta^{4+} and ii) in agreement with the lower nitrogen content the VBM of $La_{1-x}Y_xTaO_2N$ is shifted to a higher potential. Based on the data given in Tab. S9 none of the lanthanum containing materials would meet the requirements of overall solar water splitting because the potential of the VBM is lower than the redox potential of O_2/H_2O. In contrast, DFT calculations are showing a different situation for $LaTaON_2$, since there the potential of the VBM is much higher at about 1.8 V clearly exceeding the 1.23 V of water oxidation reaction. Consequently, the CBM position is also at much higher potential (even being slightly positive, ca. 0.1 V), hence, not suitable for water reduction reaction.[16] The calculated band edge positions for $CaTaO_2N$ are showing as well an offset towards a higher potential by about 0.5 V in comparison with the model using the absolute electronegativity.[15,16]

Tab. S9. Calculated band edge positions of $La_{1-x}Y_xTaO_2N$, $LaTaON_2$, and $CaTaO_2N$.

Material	E_{CBM} (V)	E_{VBM} (V)
$LaTaO_2N$	–1.20	0.70
$La_{0.9}Y_{0.1}TaO_2N$	–1.19	0.73
$La_{0.75}Y_{0.25}TaO_2N$	–1.17	0.79
$La_{0.7}Y_{0.3}TaO_2N$	–1.21	0.67
$LaTaON_2$	–1.28	0.52
$CaTaO_2N$	–0.94	1.49
$CaTaO_2N$[15]	–0.88	1.55
$CaTaO_2N$[16]	~–0.40	~1.90

So, to conclude it is still an open question if the band edge positions of $LaTa^{V}ON_2$ and $La_{1-x}Y_xTa^{IV}O_2N$ meet the requirements for overall solar water splitting because the obtained results deviate from each other depending on the applied method of determination. Keeping the observed offset of ca. 0.5 V in mind the materials might be suitable.

Crystal structure and optical bandgap analysis of Y–Ta–O and Y–Ta–O–N phases

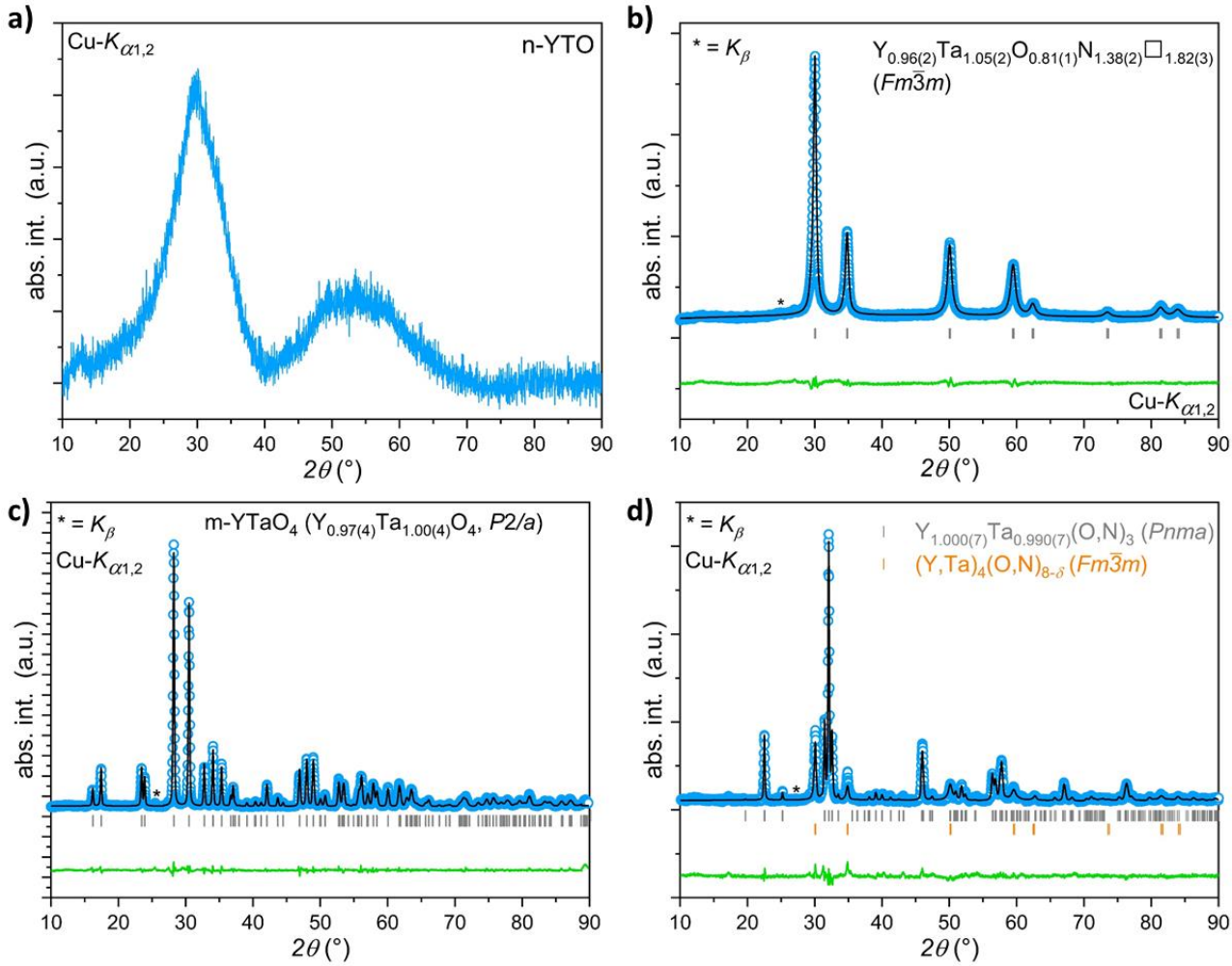

Fig. S10. a) Diffraction pattern of n-YTO. As expressed by the very large full width at half maximum (FWHM) of ca. 10° of the Bragg reflections n-YTO contains very small crystallites (nanocrystallites). b) Rietveld refinements of defect-fluorite-type phase. c) Rietveld refinements of m-$YTaO_4$ (synthesized at 1473 K) and d) Rietveld refinements of the mixture of perovskite-type phase and defect-fluorite-type phase ($YTa(O,N,\square)_4$) obtained after several *ex situ* ammonolysis cycles.

Tab. S10. a) Unit cell parameters of $Y_{0.96(2)}Ta_{1.05(2)}O_{0.81(1)}N_{1.38(2)}\square_{1.82(3)}$, $Y_{0.97(4)}Ta_{1.00(4)}O_4$, $Y_{1.000(7)}Ta_{0.990(7)}(O,N)_3$, and $YTa(O,N,\square)_4$ from PXRD data.

Unit Cell Parameter	$Y_{0.96(2)}Ta_{1.05(2)}O_{0.81(1)}N_{1.38(2)}\square_{1.82(3)}$	$Y_{0.97(4)}Ta_{1.00(4)}O_4$	$Y_{1.000(7)}Ta_{0.990(7)}(O,N)_3$	$YTa(O,N,\square)_4$
a **(Å)**	5.1536(2)	5.2942(5)	5.6851(4)	5.1464(4)
b **(Å)**	≡ *a*	5.4646(5)	7.8795(9)	≡ *a*
c **(Å)**	≡ *a*	5.1070(5)	5.4954(6)	≡ *a*
V_{cell} **(Å³)**	136.88(7)	146.86(2)	246.17(4)	136.31(2)
Space group	$Fm\bar{3}m$	$P2/a$	$Pnma$	$Fm\bar{3}m$
Phase fraction (wt.-%)	100	100	82(2)	18(2)
R_p **(%)**	5.78	6.33	7.89	
R_{wp} **(%)**	7.18	8.1	10.3	
χ^2	1.74	1.98	3.57	
R_{Bragg} **(%)**	6.18	7.62	7.96	18.4

Tab. S10. b) Refined atom positions of $Y_{0.96(2)}Ta_{1.05(2)}O_{0.81(1)}N_{1.38(2)}\square_{1.82(3)}$ from PXRD data (space group: $Fm\bar{3}m$).

Atom	Wyck. Symb.	*x*	*y*	*z*	B_{iso} (Å²)	sof.[a]
Y	4*a*	0	0	0	2[b]	0.5[c]
Ta	4*a*	0	0	0	2[b]	0.5[c]
O	8*c*	¼	¼	¼	1.5[b]	0.2025[d]
N	8*c*	¼	¼	¼	1.5[b]	0.34375[d]

[a]site occupancy factor, [b]fixed, [c]adopted from Rooksby *et al.*[17], [d]fixed according to HGE

Tab. S10. c) Refined atom positions of $Y_{0.97(4)}Ta_{1.00(4)}O_4$ (synthesized at 1473 K) from PXRD data (space group: *P*2/*a*).

Atom	Wyck. Symb.	*x*	*y*	*z*	B_{iso} (Å²)	sof.[a]
Ta	2*f*	¼	0.3059(4)	½	3.12(2)	0.505(2)
Y	2*e*	¼	0.7672(6)	0	3.01(2)	0.491(2)
O(1)	4*g*	0.505(4)	0.438(2)	0.256(3)	3.290(7)	1[b]
O(2)	4*g*	0.091(3)	0.083(2)	0.248(3)	4.26(2)	1[b]

[a]site occupancy factor, [b]fixed

Tab. S10. d) Refined atom positions of $Y_{1.000(7)}Ta_{0.990(7)}(O,N)_3$ from PXRD data (space group: *Pnma*). Due to the unknown N content and the virtually equal atomic form factors of O^{2-} and N^{3-} the refinements were carried out only using O^{2-} as anion.

Atom	Wyck. Symb.	*x*	*y*	*z*	B_{iso} (Å²)	sof.[a]
Y	4*c*	0.449(1)	¼	0.013(3)	3.3(2)	1.000(7)[b]
Ta	4*b*	0	0	0	2.1(1)	0.990(7)[b]
O(1)	4*c*	0.498(8)	¼	0.623(7)	1.5[c]	1[c]
O(2)	8*d*	0.136(4)	1.047(4)	0.279(6)	1.5[c]	1[c]

[a]site occupancy factor, [b]constrained, [c]fixed

Tab. S10. e) Refined atom positions of $YTa(O,N,\square)_4$ from PXRD data (space group: $Fm\bar{3}m$). Due to the unknown N content and the virtually equal atomic form factors of O^{2-} and N^{3-} the refinements were carried out only using O^{2-} as anion.

Atom	Wyck. Symb.	*x*	*y*	*z*	B_{iso} (Å²)	sof.[a]
Y	4*a*	0	0	0	2[b]	0.5[c]
Ta	4*a*	0	0	0	2[b]	0.5[c]
O	8*c*	¼	¼	¼	12[b]	0.55[d]

[a]site occupancy factor, [b]fixed, [c]adopted from Rooksby *et al.*[17], [d]fixed according to composition of $YTa(O,N,\square)_4$ produced from n-YTO.

DRS spectra of yttrium tantalum oxynitride

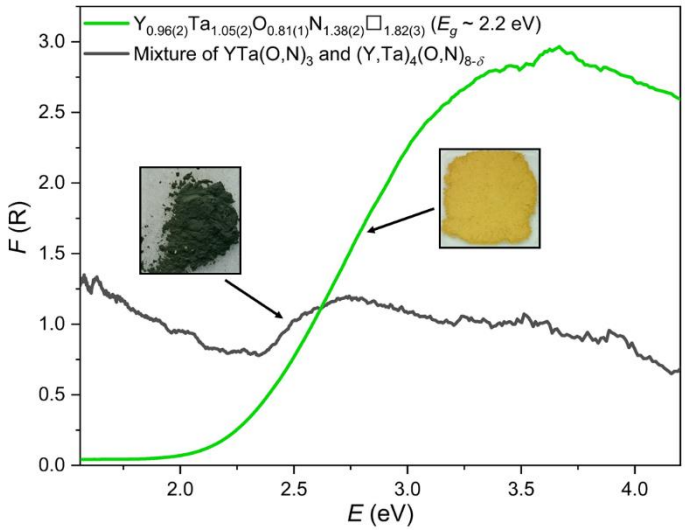

Fig. S11. Diffuse reflectance spectra - converted according to Kubelka-Munk[6] - of $Y_{0.96(2)}Ta_{1.05(2)}O_{0.81(1)}N_{1.38(2)}\square_{1.82(3)}$ and the mixture of $YTa(O,N)_3$ and $YTa(O,N,\square)_4$.

Composition of $La_{1-x}Y_xTaO_2N$ (x = 0.1, 0.25, 0.3), n-YTO, and defect-fluorite phase

Tab. S11. Weight fractions of the respective constituents of $La_{1-x}Y_xTaO_2N$ (x = 0.1, 0.25, 0.3), n-YTO, and $Y_{0.96(2)}Ta_{1.05(2)}O_{0.81(1)}N_{1.38(2)}\square_{1.82(3)}$ determined *via* ICP-OES and HGE.

Element	$La_{0.9}Y_{0.1}TaO_2N$	$La_{0.75}Y_{0.25}TaO_2N$	$La_{0.7}Y_{0.3}TaO_2N$	n-YTO	$Y_{0.96(2)}Ta_{1.05(2)}O_{0.81(1)}N_{1.38(2)}\square_{1.82(3)}$
La (wt.-%)	33.2 ± 0.4	28.2 ± 0.3	26.1 ± 0.4		
La	0.90(9)	0.76(6)	0.70(2)		
Y (wt.-%)	2.05 ± 0.08	5.03 ± 0.07	6.95 ± 0.08	26.4 ± 0.3	28.6 ± 0.3
Y	0.08(8)	0.21(4)	0.29(2)	1.00(4)	0.96(2)
Ta (wt.-%)	47.7 ± 0.5	48.9 ± 0.5	48.7 ± 0.5	54.2 ± 0.6	60.5 ± 0.7
Ta	1.00(3)	1.02(1)	1.00(6)	0.99(6)	1.05(2)
O (wt.-%)	8.74 ± 0.1	8.91 ± 0.1	8.89 ± 0.09	19.3 ± 0.2	4.12 ± 0.05
O	1.98(6)	1.96(6)	1.91(9)	4.04(4)	0.81(1)
N (wt.-%)	3.88 ± 0.04	3.91 ± 0.04	4.38 ± 0.05		6.16 ± 0.08
N	1.01(4)	1.03(4)	1.08(1)		1.38(2)

X-Ray photoelectron spectroscopy – survey spectra

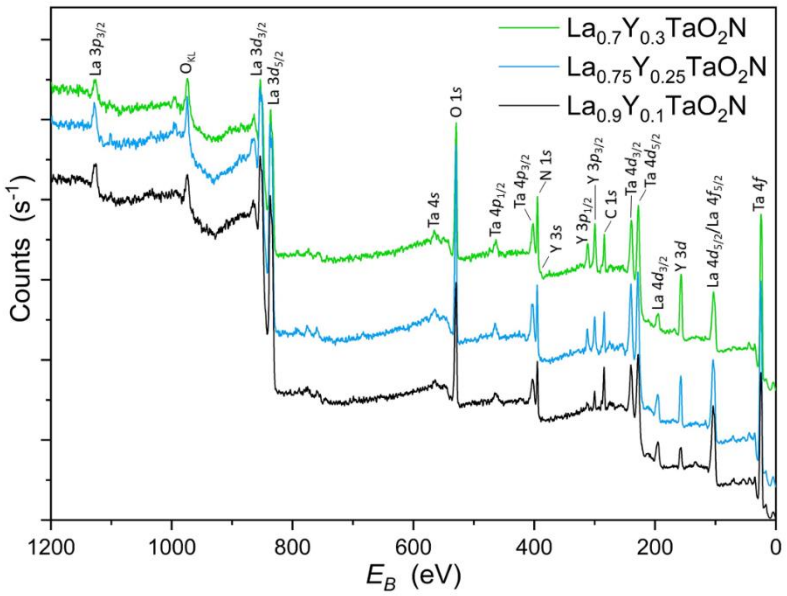

Fig. S12. XPS survey spectra of $La_{1-x}Y_xTaO_2N$ (x = 0.1, 0.25, 0.3).

Magnetic behavior

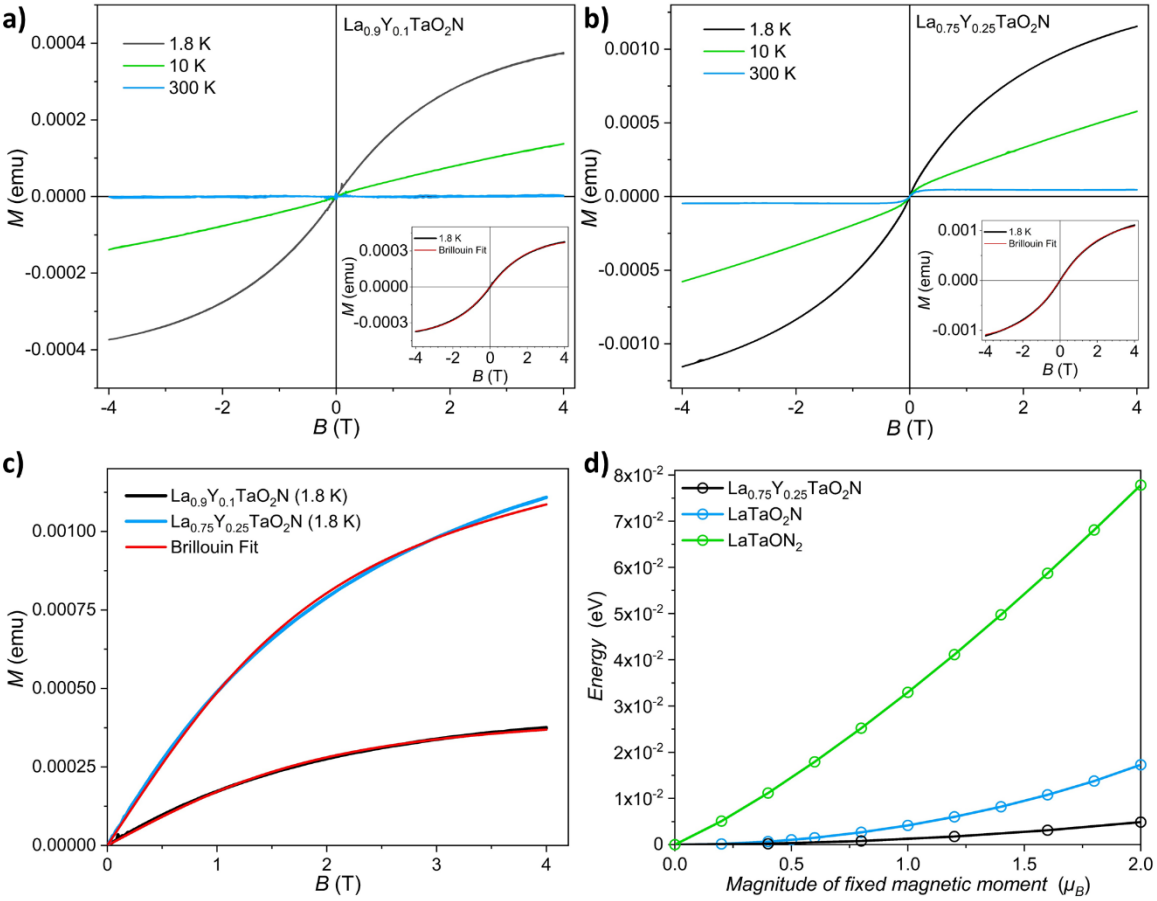

Fig. S13. Temperature dependent M vs. H plots of a) $La_{0.9}Y_{0.1}TaO_2N$ and b) $La_{0.75}Y_{0.25}TaO_2N$. No coercive fields are observed for both compounds pointing to a very tiny paramagnetic contribution at very low temperatures (1.8 K). The insets show the pure 1.8 K paramagnetic contribution, where the room temperature curves have been subtracted, to remove visible but small room temperature ferromagnetic behavior. c) Brillouin fits of $La_{0.9}Y_{0.1}TaO_2N$ and $La_{0.75}Y_{0.25}TaO_2N$. d) Total energies as a function of the magnetic moment μ_B for $LaTaON_2$, $LaTaO_2N$, and $La_{0.75}Y_{0.25}TaO_2N$.

Electronic band structure

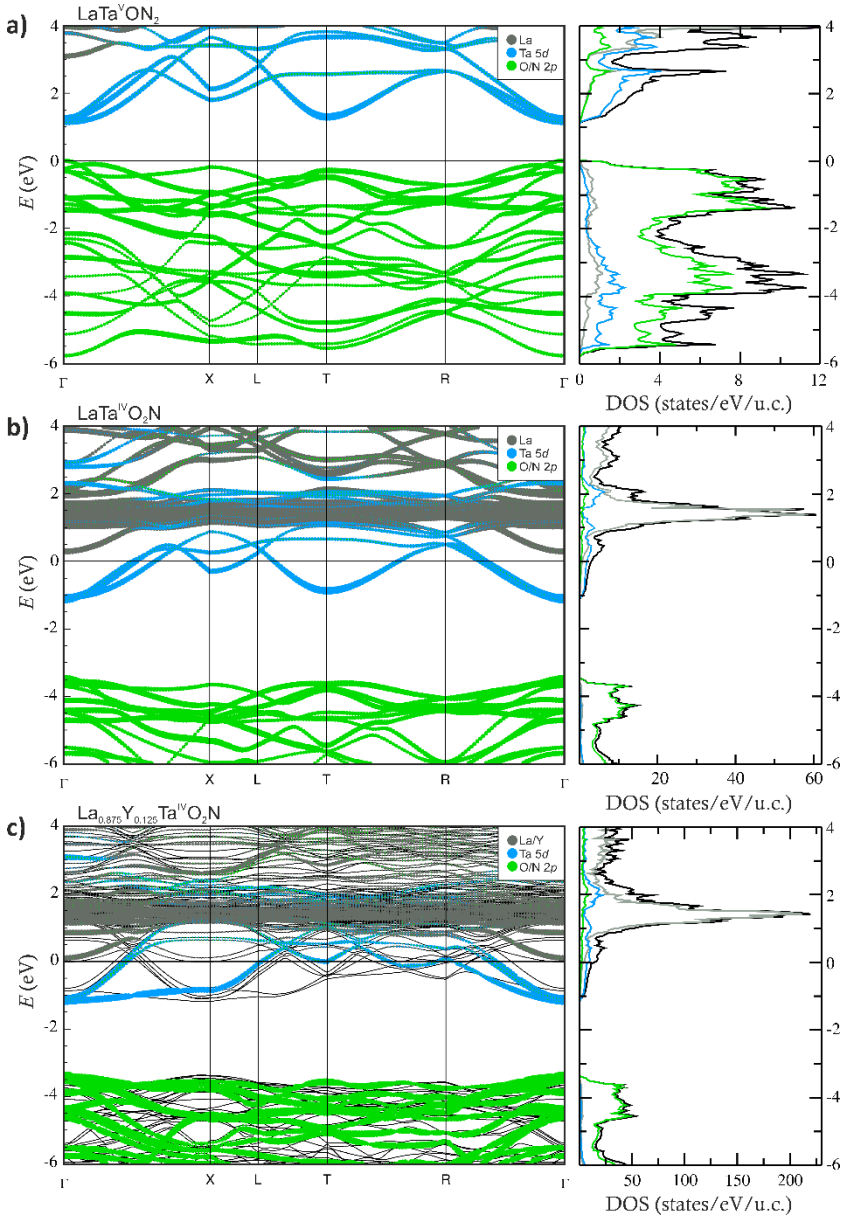

Fig. S14. Electronic band structure of a) $LaTaON_2$, b) $LaTaO_2N$ and c) $La_{0.875}Y_{0.125}TaO_2N$ showing the metallic nature of the Ta 5*d* levels of $La_{1-x}Y_xTaO_2N$ and the direct bandgap of $LaTaON_2$.

A change of the charge carrier excitation behavior between $LaTa^{V}ON_2$ and $La_{1-x}Y_xTa^{IV}O_2N$ is implied by the electronic band structures shown in Fig. S14. A classical semiconductor-like band structure is observed for $LaTaON_2$ (Fig. S14 b)) showing an electronic excitation from the valence band (VB) formed by O/N 2*p* states across the bandgap to the empty Ta 5*d* states in the conduction band (CB). The calculated bandgap is about 1.1 eV showing the typical underestimation of DFT calculations in comparison to the experimental optical bandgap of 1.8 eV.[1] For $La_{1-x}Y_xTaO_2N$ (Fig. S14 a) and c)) the assignment of VB and CB and transition of electrons during excitation is due to its metallic character not straightforward anymore because the highest occupied state is no longer located in the VB. Based on the determined optical bandgaps and the calculated electronic band structure of $La_{1-x}Y_xTaO_2N$ the excitation is not occurring from O/N 2*p* states (as in $LaTaON_2$) to the empty states in the CB. The calculated energetic difference is with ca. 2.5 eV (Γ-point) clearly larger than the experimental bandgap. Additionally, the fact that most DFT calculations underestimate bandgaps must be recalled. Therefore, an excitation from the partly occupied Ta 5d states to energetically higher empty levels seems to be responsible for the visible-light absorption. This transition shows a very similar offset between calculated (ca. 1.4 eV) and experimental (1.88 eV – 1.96 eV) bandgap as observed for $LaTaON_2$. A similar behavior was previously described for the red metallic oxide photocatalyst $Sr_{1-x}NbO_3$.[18]

Surface photovoltage spectroscopy

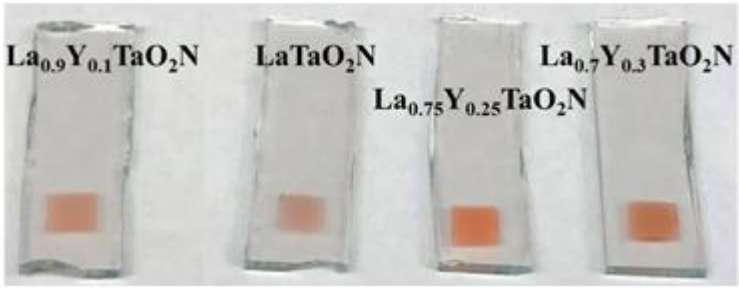

Fig. S15. $La_{1-x}Y_xTaO_2N$ (x = 0.1, 0.25, 0.3) films for SPS measurements.

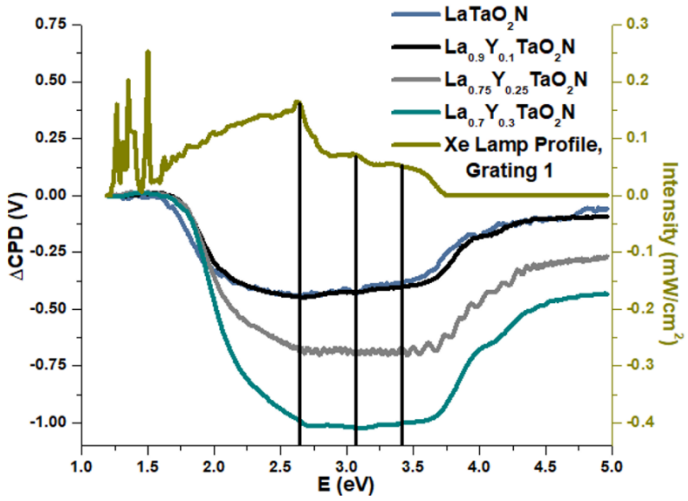

Fig. S16. SPS data for $La_{1-x}Y_xTaO_2N$ powder samples on FTO overlaid with the emission spectrum of the xenon lamp used for the measurements.

Tab. S12. Summary of SPS photo-onsets, estimated effective bandgaps, maximum photovoltage values, surface area by BET method, film thicknesses, and times for photovoltage formation and decay. Time constants τ_{on} and τ_{off} show the time required to reach 63.21% of the final photovoltage after turning the light on or off.

Material	Photo-onset (eV)	Effective $E_{G,eff}$ (eV)	Max ΔCPD (V)	S_{BET} (m^2/g)	Avg. Film Thickness (nm)	τ_{on} (s)	τ_{off} (s)
$LaTaO_2N$	1.58	1.65	-0.44	8.0	879 ± 167	21.91	89.46
$La_{0.9}Y_{0.1}TaO_2N$	1.68	1.74	-0.45	20.4	1315 ± 227	7.62	73.39
$La_{0.75}Y_{0.25}TaO_2N$	1.68	1.78	-0.69	21.1	1210 ± 190	10.65	205.96
$La_{0.7}Y_{0.3}TaO_2N$	1.64	1.78	-1.01	27.9	1526 ± 378	20.71	242.66

Supplementary References

1 C. Bubeck, M. Widenmeyer, G. Richter, M. Coduri, E. Goering, S. Yoon and A. Weidenkaff, *Commun. Chem.*, 2019, **2**, 134.

2 G. S. Henderson, F. M. F. De Groot and B. J. A. Moulton, *Rev. Mineral. Geochemistry*, 2014, **78**, 75–138.

3 M. Widenmeyer, C. Peng, A. Baki, W. Xie, R. Niewa and A. Weidenkaff, in *Solid State Sciences*, 2016, vol. 54, pp. 7–16.

4 C. M. Leroy, A. E. Maegli, K. Sivula, T. Hisatomi, N. Xanthopoulos, E. H. Otal, S. Yoon, A. Weidenkaff, R. Sanjines and M. Grätzel, *Chem. Commun.*, 2012, **48**, 820.

5 D. Logvinovich, J. Hejtmánek, K. Knižek, M. Maryško, N. Homazava, P. Tomeš, R. Aguiar, S. G. Ebbinghaus, A. Reller and A. Weidenkaff, *J. Appl. Phys.*, 2009, **105**, 023522.

6 G. Kortüm, W. Braun and G. Herzog, *Angew. Chemie Int. Ed. English*, 1963, **2**, 333–341.

7 T. A. Kurova and V. B. Aleksandrov, *Dokl. Akad. Nauk SSSR*, 1971, **201**, 1095–1098.

8 Y. O. Titov, A. M. Sich, V. Y. Markiv, N. M. Belyavina, A. O. Kapshuk and M. S. Slobodyanik, *Dopovidi Natsional'noi Akad. Nauk Ukr.*, 2003, **3**, 140–145.

9 L. H. Brixner and H. Y. Chen, *J. Electrochem. Soc.*, 1983, **130**, 2435–2443.

10 S. H. Porter, Z. Huang and P. M. Woodward, *Cryst. Growth Des.*, 2014, **14**, 117–125.

11 L. Clark, J. Oró-Solé, K. S. Knight, A. Fuertes and J. P. Attfield, *Chem. Mater.*, 2013, **25**, 5004–5011.

12 E. Günther, R. Hagenmayer and M. Jansen, *Z. Anorg. Allg. Chem.*, 2000, **626**, 1519–1525.

13 Laurence M. Peter, in *Photocatalysis: Fundamentals and Perspectives*, The Royal Society of Chemistry, 2016, pp. 1–28.

14 Y. Xu and M. A. A. Schoonen, *Am. Mineral.*, 2000, **85**, 543–556.

15 J. Xu, C. Pan, T. Takata and K. Domen, *Chem. Commun.*, 2015, **51**, 7191–7194.

16 I. E. Castelli, D. D. Landis, K. S. Thygesen, S. Dahl, I. Chorkendorff, T. F. Jaramillo and K. W. Jacobsen, *Energy Environ. Sci.*, 2012, **5**, 9034–9043.

17 H. P. Rooksby and E. A. D. White, *J. Am. Ceram. Soc.*, 1964, **47**, 94–96.

18 X. Xu, C. Randorn, P. Efstathiou and J. T. S. Irvine, *Nat. Mater.*, 2012, **11**, 595–598.